DESIGN AND PERFORMANCE OF HIGH LASER POWER INTERFEROMETERS FOR
GRAVITATIONAL-WAVE DETECTION

By

KATHERINE L DOOLEY

A DISSERTATION PRESENTED TO THE GRADUATE SCHOOL
OF THE UNIVERSITY OF FLORIDA IN PARTIAL FULFILLMENT
OF THE REQUIREMENTS FOR THE DEGREE OF
DOCTOR OF PHILOSOPHY

UNIVERSITY OF FLORIDA

2011

My dedication.

ACKNOWLEDGMENTS

Some personal acknowledgements–professors, fellow grad students, friends, family.

Acknowledgments for the funding of LIGO.

And David Feldbaum says I must include a thank you for him because I made him search the elog for a spiricon BCS picture one too many times for me.

TABLE OF CONTENTS

LIST OF TABLES

LIST OF FIGURES

LIST OF SYMBOLS, NOMENCLATURE, AND ABBREVIATIONS

ASC   Angular Sensing and Control

EOM   electro-optic modulator

FI   Faraday isolator

GW   gravitational wave

IO   Input Optics

LIGO   Laser Interferometer Gravitational-wave Observatory

LSC   length sensing and control

MC   mode cleaner

MMT   mode matching telescope

PSL   pre-stabilized laser

PRC   power recycling cavity

REFL   reflected beam

RF   radio frequency

RM   recycling mirror

TGG   Terbium Gallium Garnate

TM   test mass

VIRGO Variability of Solar Irradiance and Gravity Oscillations

WFS   wave-front sensor

Abstract of dissertation Presented to the Graduate School
of the University of Florida in Partial Fulfillment of the
Requirements for the Degree of Doctor of Philosophy

DESIGN AND PERFORMANCE OF HIGH LASER POWER INTERFEROMETERS FOR
GRAVITATIONAL-WAVE DETECTION

By

Katherine L Dooley

September 2011

Chair: David Reitze
Major: Physics

My abstract.

CHAPTER 1
THE SEARCH FOR GRAVITATIONAL WAVES

1.1   Introduction

The field of ground-based gravitational-wave (GW) physics is rapidly approaching a state with a high likelihood of detecting GWs for the first time. Such a detection will not only validate part of Einstein's general theory of relativity, but initiate an era of astrophysical observation of the universe through GWs. Gravitational waves are generated by non-axisymmetric acceleration of mass and travel in the medium of space-time at the speed of light. The frequency of the gravitational wave depends on its source. A first detection is expected to witness an event such as a supernova or binary black hole/neutron star merger.

1.2   The theory of gravitational radiation

Gravitational radiation is a perturbation $|h_{\mu\nu}| \ll 1$ to the flat space-time Minkowski metric $\eta_{\mu\nu} = \text{diag}(-1,1,1,1)$. The metric describing space-time in the presence of gravitational radiation is therefore

$$g_{\mu\nu} = \eta_{\mu\nu} + h_{\mu\nu}. \tag{1.2.1}$$

Just as in electrodynamics where one has freedom in choosing the vector potential $\vec{A}$ for calculating the magnetic field $\vec{B} = \vec{\nabla} \times \vec{A}$, one also has freedom in general relativity in choosing the form of $h_{\mu\nu}$ for ease of calculation. A convenient and popular choice is called the transverse-traceless (TT) gauge in which

$$h_{\mu\nu} = \begin{bmatrix} 0 & 0 & 0 & 0 \\ 0 & h_+ & h_\times & 0 \\ 0 & h_\times & -h_+ & 0 \\ 0 & 0 & 0 & 0 \end{bmatrix} \tag{1.2.2}$$

where the $+$ and $\times$ represent two linearly independent polarizations. Without loss of generality, we consider the h_+ polarization in the example that follows.

For a gravitational wave traveling along the z axis, the metric is given by:

$$ds^2 = -c^2 dt^2 + [1 + h_+(t)]dx^2 + [1 - h_+(t)]dy^2. \tag{1.2.3}$$

This says the TT coordinate system is stretched along the x axis and and compressed along the y axis by a factor of

$$\sqrt{1 \pm h_+(t)} \approx 1 \pm \frac{1}{2} h_+(t).$$ (1.2.4)

Therefore, the *proper distance* between two free masses located along either the x or the y axes changes by the factor in Eq. 1.2.4; their coordinate separations remain constant. The GW perturbation is a dimensionless strain

$$h = 2\frac{\Delta L}{L}.$$ (1.2.5)

1.3   Sources

Any object with an accelerating mass quadrupole moment generates gravitational waves. The typical strain amplitudes, however, are extremely tiny: a binary system of coalescing 1M$_\odot$ neutron stars in the Virgo Cluster (a distance of 15 Mpc) would produce a maximum GW strain on Earth of only 10^{-21}. The strain is proportional to source mass and velocity, and inversely proportional to distance from the observer:

$$h \approx \frac{GMv^2}{Rc^4}$$ (1.3.1)

Consequently, the most promising sources of detectable gravitational waves are nearby, fast-moving, massive astrophysical objects that include

- supernovae
- binary stars (orbiting or coalescing)
- spinning neutron stars
- cosmological/astrophysical background

and can be categorized as producing periodic, burst, or stochastic GWs.

Stably orbiting binary star systems comprised of black holes or neutron stars as well as rapidly spinning non-axisymmetric pulsars are considered periodic sources since they will produce GWs of relatively constant frequency. These reliable sources of GWs require a long integration time to pick out their signal above noise. The Hulse-Taylor binary, for instance, falls into this category. Supernovae are burst sources since the gravitational collapse will produce a

short-lived, unmodeled emission of GWs. Binaries in their final tens of milliseconds of inspiral also fall into this category. Finally, the anisotropies in the inflation of the universe together with the hum of all distant astrophysical sources will create a stochastic background of radiation. Coherent cross-correlation between multiple detectors is necessary for measuring the constant amplitude, broad-spectrum GW background.

Directly detecting gravitational radiation from any such source will reveal information that electromagnetic radiation cannot convey. The frequency of the GW tells about the dynamical timescale of the source. Only through GW radiation, for example, can mass and spin properties of a black hole be revealed.

1.4   Methods of detection

- Hulse/Taylor

- Resonant bars

- Pulsar timing

- CMB polarization (B-modes)

- Interferometry

For an approachable overview of the history of the field, including detector design choices and estimated GW strain amplitudes of various sources, refer to Ref. [1].

1.5   State of ground-based interferometry

A network of first generation kilometer scale laser interferometer gravitational-wave detectors completed its integrated 2-year data collection run in 2007, called S5. The instruments were: the American Laser Interferometer Gravitational-wave Observatories (LIGO)[2], one in Livingston, LA with 4 km long arms and two in Hanford, WA with 4 km and 2 km long arms; the 3 km French-Italian detector VIRGO[3] in Cascina, Italy; and the 1.2 km German-British detector GEO[4] in Ruthe, Germany. Multiple separated detectors increase detection confidence through signal coincidence and improve source localization through triangulation.
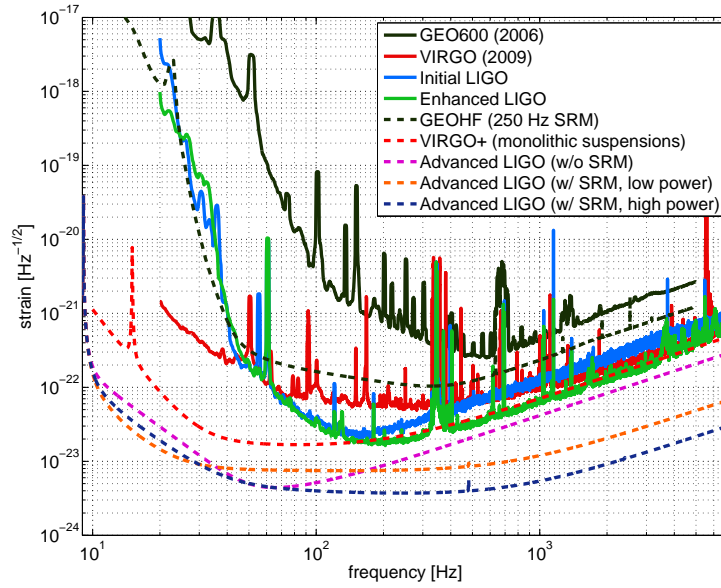
Figure 1-1. Strain sensitivities of LIGO-VIRGO collaboration interferometers.

The first generation of LIGO, known as Initial LIGO, achieved its design goal of sensitivity to GWs in the 40 Hz - 7000 Hz band which included an impressive record strain sensitivity of $2 \times 10^{-23}/\sqrt{\text{Hz}}$ at 155 Hz. However, only the loudest of sources produce enough GW strain to appear in LIGO's band, and no gravitational wave has yet to be found in the S5 data. A second generation of LIGO detectors, Advanced LIGO, has been designed to be at least an order of magnitude more sensitive at several hundred Hz and above and include an impressive increase in bandwidth down to 10 Hz, dramatically increasing the chances of detection. To test some of Advanced LIGO's new technologies, an incremental upgrade to the detectors was carried out after S5 [5]. This project, Enhanced LIGO, culminated with the S6 science run from July 2009 to October 2010. Currently, construction of Advanced LIGO is underway. VIRGO and GEO will both undergo their own upgrades as well [3] [6]. See Figure 1-1 for achieved and theoretical noise curves.

The baseline Advanced LIGO design [7] improves upon Initial LIGO by featuring better seismic isolation, the addition of a signal extraction mirror at the output port, homodyne readout,

and an increase in laser power from 10 W to 200 W. The substantial increase in laser power improves the shot-noise-limited sensitivity, but introduces a host of radiation pressure and thermally induced side effects that must be addressed for proper operation.

The recently completed Enhanced LIGO tested portions of the Advanced LIGO designs so unforeseen difficulties could be addressed and so that a more sensitive data taking run could take place. An output mode cleaner was designed, built and installed, and DC readout of the GW signal was implemented [8]. An Advanced LIGO active seismic isolation table was also built, installed, and tested [9]. In addition, the 10 W Initial LIGO laser was replaced with a 35 W laser [10]. Accompanying the increase in laser power, both the Alignment Sensing and Control and Input Optics were modified. The upgrades of these two subsystems make up the content of this dissertation.

1.6 Purpose of this work

The purpose of this work is to demonstrate the capability of an interferometric gravitational wave detector to operate at several times the highest of laser powers previously used. To first order, more power is desirable since strain sensitivity improves by $\sqrt{P}$ in the high frequency ($>$ several hundred Hz) shot-noise-limited region. However, as detectors become more sensitive at low frequencies (< 100 Hz), radiation pressure noise will become the dominant noise source, making high laser power operation a design trade-off. Currently, since seismic noise limits low frequency sensitivity, exploring the technical world of increasing the laser power is a fruitful adventure.

Operation of Initial LIGO was limited to 7 W input power due to uncontrolled radiation pressure torque instabilities in the arm cavities. Explained theoretically by Sidles and Sigg [11], measured experimentally by Hirose [12], and modeled by Barsotti [13], the effect of radiation pressure torque on angular alignment needed to be addressed in practice in order for Enhanced LIGO to succeed in operating at its design power of 30 W. We present the re-designed Angular Sensing and Control system as implemented on the Enhanced LIGO detectors and show

results of its performance with up to 20 W input power, demonstrating good agreement between experiment and model.

Additional complications of high laser power operation arise from thermal effects. Absorption of power by optical components induces thermal lensing which changes the properties of the propagating laser. The Input Optics, which condition the laser for optimal use in the interferometer, suffered from thermal absorption of the 7 W of Initial LIGO. Although not a source of GW strain noise, the thermal performance of the Input Optics must be good enough so as to not hinder

CHAPTER 2
LASER INTERFEROMETERS FOR GRAVITATIONAL-WAVE DETECTION

2.1 Introduction

The typical detector configuration is a power-recycled Fabry-Perot Michelson laser interferometer featuring suspended test masses in vacuum as depicted in Figure 2-1. A diode-pumped, power amplified, and intensity and frequency stabilized Nd:YAG laser emits light at 1064 nm. The laser is directed to a Michelson interferometer whose two arm lengths are set to maintain destructive interference of the recombined light at the anti-symmetric (AS) port. An appropriately polarized gravitational wave will differentially change the arm lengths, producing signal at the AS port proportional to the GW strain and the input power. The Fabry-Perot cavities in the Michelson arms and a power recycling mirror (RM) at the symmetric port are two modifications to the Michelson interferometer that increase the laser power in the arms and therefore improve the detector's sensitivity to GWs.

2.2 Measuring GW strain with light

2.2.1 Light as a photon

Consider two wave packets leaving the beam splitter of a Michelson interferometer at the same time, each heading down a different arm. If an appropriately polarized gravitational wave is present, the amount of time the wave packet takes to travel down a stretched arm and back is:

$$t_{rt+} = \frac{2L}{c}\left(1 + \frac{h_+}{2}\right) \tag{2.2.1}$$

Likewise, for a compressed arm the roundtrip travel time is:

$$t_{rt-} = \frac{2L}{c}\left(1 - \frac{h_+}{2}\right) \tag{2.2.2}$$

There is a non-zero $2Lh_+/c$ difference in arrival times at the beam splitter, a quantity one could measure with an accurate stationary clock. This demonstrates intuitively that a laser interferometer can detect gravitational waves.
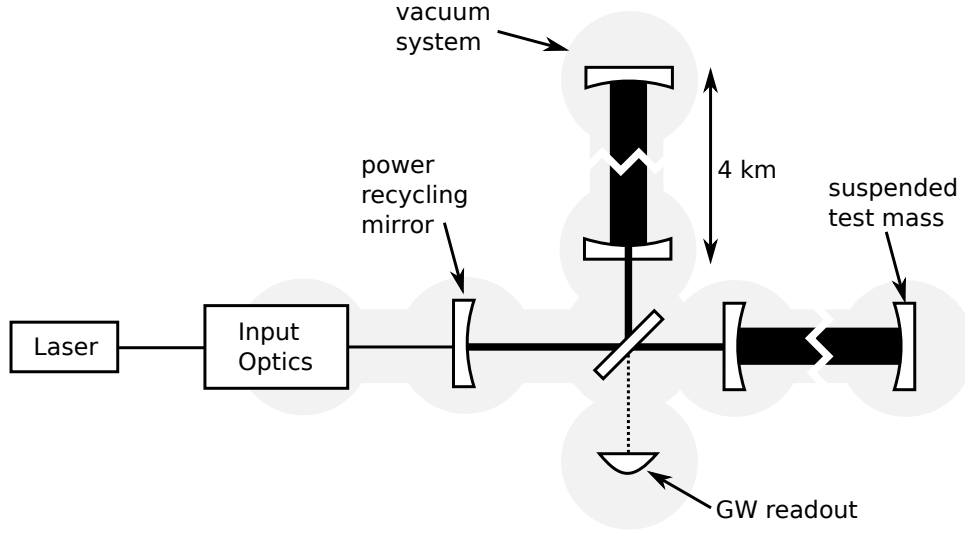
Figure 2-1. Power-recycled Fabry-Perot Michelson laser interferometer.

It should be noted that we had to use the approximation that the gravitational wave wavelength λ_{gw} is much larger than the interferometer arm length L. This means that the temporal variation of $h_+(t)$ is negligible during the time it takes the photon to make its roundtrip. Thus, h_+ is treated as a constant in Eqs. 2.2.1 and 2.2.2.

2.2.2 Light as a wave

The detector at the beam splitter is not a clock, but a photodetector which is sensitive to phase. It would be informative, therefore, to express the difference in arrival times as a difference in phase. To do so, we must move away from the photon model and think about the wave model of light. The light wave's phase is given by $\phi = \omega t$ where t is the proper time. Then, the difference in phase between the two light beams after each has completed its roundtrip is:

$$\Delta\phi = \phi_{rt+} - \phi_{rt-} = \frac{2L\omega}{c}h_+ \tag{2.2.3}$$

Two time derivatives yields

$$\frac{d^2\Delta\phi}{dt^2} = \frac{2L\omega}{c}\partial_t\partial_t h_+. \tag{2.2.4}$$

It can be shown [14] that the Riemann tensor in the TT gauge is $R_{tkti} = -\frac{1}{2}\partial_t\partial_t h_{ki}$, and gauge invariant. Therefore, our physically measurable quantity can be expressed as being manifestly gauge invariant, proving that a laser interferometer can detect the effect of gravitational waves.

2.3   Signal versus noise

The factors that must be considered in the design of any detector can be grouped into two categories: signal and noise. The ability to make a claim of detection is largely dependent on the magnitude of the signal to noise ratio. For laser interferometers, the strength of the GW signal is proportional to the length of the arms and the amount of power in the arms. (See Eq. **??**.) Therefore, the two primary fundamental ways to make a GW produce a bigger signal in an interferometer are: 1) make the arms longer, and 2) increase the circulating power. The change in the distance between the mirrors, ΔL, is bigger for a given strain the longer the arms. With more circulating power, the greater the amount that will show up at the AS port for a given displacement from the dark fringe.

No matter how large a signal one might have, it won't be found confidently, or at all, if there is too much noise in the background. Interferometers for GW detection are plagued primarily by seismic noise (below 70 Hz) and shot noise (above 200 Hz). Seismic noise physically displaces the mirrors, resulting in changes in the length of the arm. Shot noise is a quantum mechanical effect of the detection of photons which creates uncertainty in the phase of the light (and therefore the power) at the AS port.

2.4   Sensitivity Limits

- Displacement noise (ground motion, thermal noise)
- Sensing noise (stray light, shot noise)

2.5   Power Recycled Michelson Interferometers

- phase detection, sidebands
- sub-systems, basic loops

2.6   More Laser Power

2.7   Digital Control in LIGO

The LIGO interferometers are interfaced through a digital control system.

CHAPTER 3
INPUT OPTICS FOR HIGH LASER POWER

3.1 Introduction

The Input Optics (IO)[1] is one of many subsystems of the LIGO interferometers. Its

purpose is to deliver an aligned, spatially pure, mode-matched beam with phase-modulation

sidebands to the power-recycled Fabry-Perot Michelson interferometer. The IO must prevent the

backscattering of light into the laser, recover the beam reflected from the interferometer for signal

detection and have high optical efficiency. It should not be a limiting noise source for DARM.

There are four major components to the Input Optics subsystem:

- electro-optic modulator (EOM)
- mode cleaner cavity (MC)
- Faraday isolator (FI)
- mode matching telescope (MMT)

A layout is shown in Fig. 3-1 and the conceptual design is found in Ref. [15]. The focus of the U.

of Florida's responsibility for the Input Optics is their design, fabrication, and performance under

high laser powers. I elaborate on those aspects of the IO in this chapter, leaving the IO noise

performance to a future discussion.

3.1.1 Problems in Initial LIGO

The Initial LIGO interferometers were equipped with a 10 W laser, yet operated with only

7 W input power due to radiation pressure induced opto-mechanical instabilities in the arm

cavities. The EOM sat before the power control in the 10 W beam and the other components saw

anywhere up to 7 W laser power. The 7 W operational limit was not due to the failure of the Input

Optics; however, the quality of the IO performance did degrade with power.

The single greatest fault of the Initial LIGO Input Optics was thermal drift in the Faraday

isolator. The FI elements produced thermal deflection of the beam, leading to a significant beam

drift between the interferometer's locked and unlocked states. The reflected beam, for instance,

---

[1] The Input Optics was originally called the Input-Output Optics (IOO).
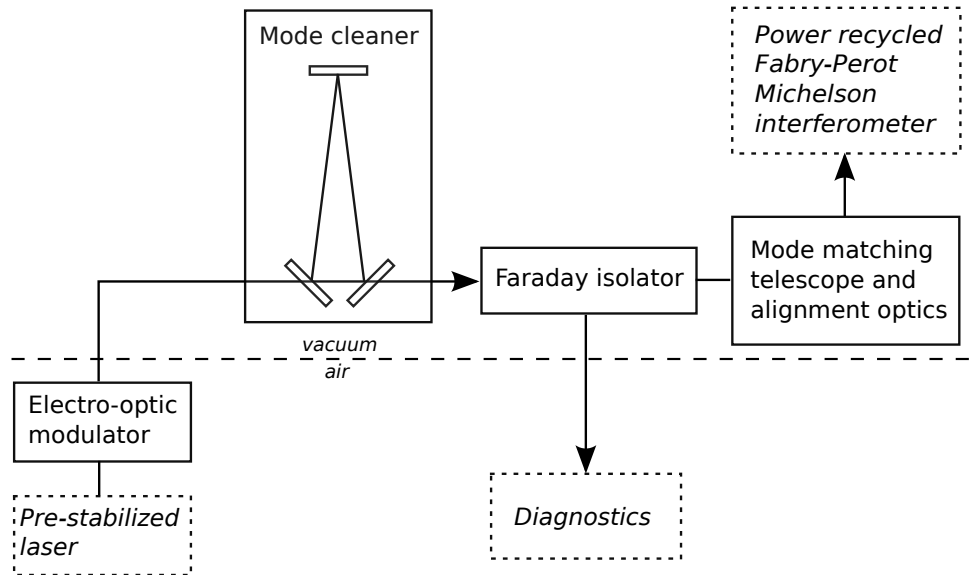
Figure 3-1. Input Optics subsystem schematic. IO components are identified by solid rectangles. Make very detailed! OptoCad drawing, perhaps?

would wander completely off of a 0.5 cm diameter sensing photodiode during the course of powering up the interferometer. Measurements estimate there was a deflection of 1 mrad at the FI. This was mitigated at the time by the design, installation, and use of the REFL beam servo (RBS), an active beam steering system on the beam rejected by the isolator.

There were also known limits to the power the IO could sustain. For example, thermal lensing in the Faraday isolator optics would start to significantly alter the beam mode at powers greater than 10 W. Additionally, the absorptive FI elements would create thermal birefringence with more power, degrading the optical efficiency and isolation. Also, the Initial LIGO electro-optic modulators had an operational power limit of around 10 W; anisotropic thermal lensing made the EOMs unsuitable for much higher power. Finally, the mode cleaner optics exhibited rather high absorption–enough such that thermal lensing of the MC optics at higher powers would degrade the mode quality of the beam and therefore its finesse. A power-dependent mode mismatch into the interferometer would also be expected.

In addition to the thermal limitations of the Initial LIGO IO, optical efficiency in delivering light from the laser into the interferometer was not optimal during Initial LIGO. Of the light

entering the Input Optics chain, only 60% remained by the time it reached the power recycling mirror. In addition, only 83% of the light reaching the interferometer was coupled into the arm cavity mode at Livingston, leaving room for improvement in the MMT design.

3.2 Design of Enhanced LIGO Input Optics

3.2.1 Electro-optic modulator

The electro-optic modulator phase modulates carrier light to produce RF sidebands that are needed for sensing the interferometer lengths and angles [16]. Carrier light with field $E_0 e^{i\omega t}$ has first order sidebands with amplitude $E_0 J_1(\Gamma_i)e^{i(\omega+\Omega_i)t} + E_0 J_{-1}(\Gamma_i)e^{i(\omega-\Omega_i)t}$ addet to it, along with infinitely many higher order sidebands of insignificant amplitude. The J are Bessel functions, Γ_i are modulation indices, and Ω_i are the modulation frequencies of 24.4 MHz, 33 MHZ and 61.2 MHz. The EOM is a resonant LC circuit made of a crystal with an electric field dependent index of refraction sandwiched between capacitor plates and attached to an inductor. The EOM is the last element the laser passes through before entering the interferometer's vacuum system.

The Enhanced LIGO EOM design uses a crystal of rubidium titanyl phosphate (RTP), which has 1/10 the absorption coefficient at 1064 nm of the lithium niobate ($LiNbO_3$) crystal used in Initial LIGO's commercially-made EOMs. The RTP has twice the damage threshold of $LiNbO_3$ and a similar electro-optic coefficient. Also, the RTP's dn/dT anisotropy is 50% smaller. Based on an RTP absorption coefficient of 50 ppm/cm as reported by Raicol, a thermal lens of 200 m and higher order mode content of less than 1% can be expected with 200 W input power. (Report for 30 W here, not 200 W.)

We procured the crystals from Raicol and packaged them into modulators. A diagram is shown in Fig. 3-2. The crystal dimensions are $4 \times 4 \times 40$ mm and their faces are wedged by $2.85°$ and AR coated. Only one crystal is used in the EOM in order to reduce the number of surface reflections. Three separate pairs of electrodes each with its own resonant LC circuit are placed across the crystal in series, producing the three required sets of RF sidebands: 24.4 MHz, 33 MHZ and 61.2 MHz. Reference [17] contains further details.
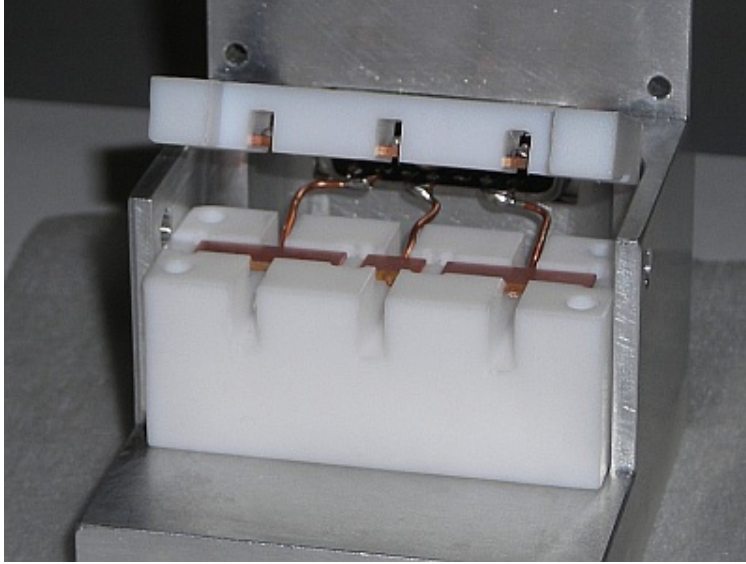
Figure 3-2. Electro-optic modulator. Make a schematic drawing (crystal + electrodes + inductors) to accompany a picture like this one.

3.2.2 Mode cleaner

The mode cleaner is a 12.2 m long suspended three mirror optical cavity with finesse $\mathscr{F} = 1282$ and free spectral range of 12.243 MHz. It is the first in-vacuum component the laser beam encounters. The MC must transmit two of the sets of sideband light, reject laser output that is not in the fundamental TEM_{00} mode, and play both a passive and active role in laser frequency stabilization [18].

3.2.3 Faraday isolator

The Faraday isolator is a three-port optical system that transmits light straight through in one direction, yet rejects light traveling in the opposite direction out of a third port. Crystals with a high Verdet constant $\mathscr{V}$ and length L sit in a magnetic field with flux density B, rotating the polarization of the light passing through by an angle $\beta = \int_0^L \mathscr{V}B(z)dz$, with z the propagation direction. Polarizers outside of the magnetic field purify the polarization of the light and send the backwards-traveling rotated light out the third port, thus protecting the laser source. This recovery of the reflected light from the interferometer is also necessary for extracting length and angular information about the interferometer's cavities. The Faraday isolator sits in the interferometer vacuum system after the mode cleaner.

The Enhanced LIGO Faraday isolator design required more than simply the use of low absorption optics. Even with minimal absorption, the residual lensing and birefringence needed to be further mitigated through additional design choices. Also, trade-offs between optical throughput in the forward direction, optical isolation in the backwards direction, and feasibility of physical access of the return beam had to be considered. The result is that the Enhanced LIGO Faraday isolator has a new layout and new optics compared to both the Initial LIGO FI and typical commercial isolators.

Figure 3-3 shows a schematic of the Enhanced LIGO Faraday Isolator. It begins and ends with calcite wedge polarizers (CWP). Between the CWPs is a thin film polarizer (TFP), a deuterated potassium dihydrogen phosphate (DKDP) element, a half-wave plate (HWP), and a Faraday rotator. The rotator is made of two low absorption terbium gallium garnet (TGG) crystals and a quartz rotator (QR) inside a 7-disc magnet with field strength of 1.16 T at its maximum. The forward propagating beam upon passing through the TGG, QR, TGG, HWP cascade is rotated by $+22.5° - 67.5° + 22.5° - 22.5° = 0°$. In the backwards direction, the rotation through HWP, TGG, QR, TGG is $-22.5° + 22.5° + 67.5° + 22.5° = 90°$.

3.2.3.1 Thermal birefringence

Thermal birefringence is addressed by the use of two TGG crystals and one quartz rotator rather than the typical single TGG. In this configuration, any thermal polarization distortions that the beam experiences while passing through the first TGG rotator will be partially compensated upon passing through the second. The multiple elements in the magnet requires a larger magnetic field than in Initial LIGO and a Faraday rotator housing that is 15.5 cm in diameter by 16.1 cm long.

3.2.3.2 Thermal lensing

Thermal lensing is addressed by including DKDP, a negative dn/dT material, in the beam path. Absorption of light in the DKDP results in a de-focusing of the beam, which compensates for the thermal focusing induced by absorption in the TGGs [19].
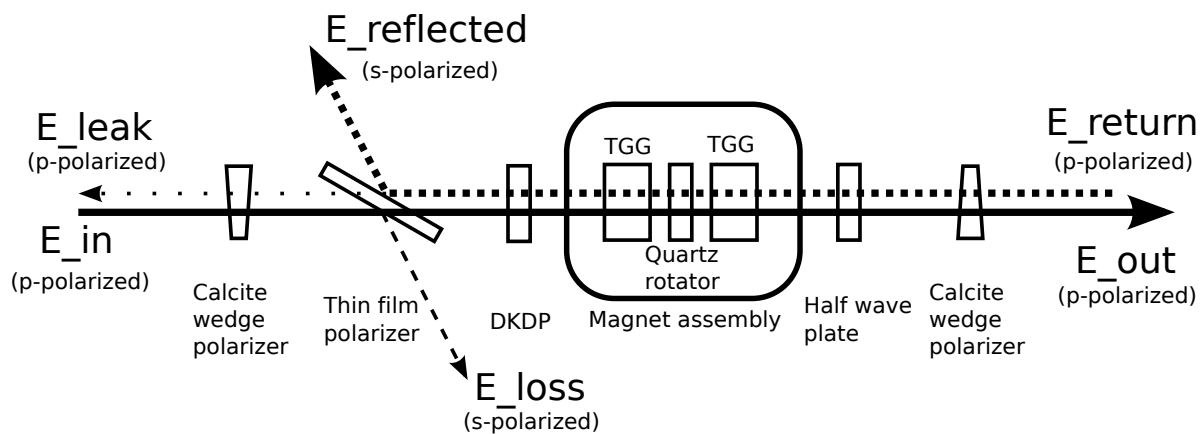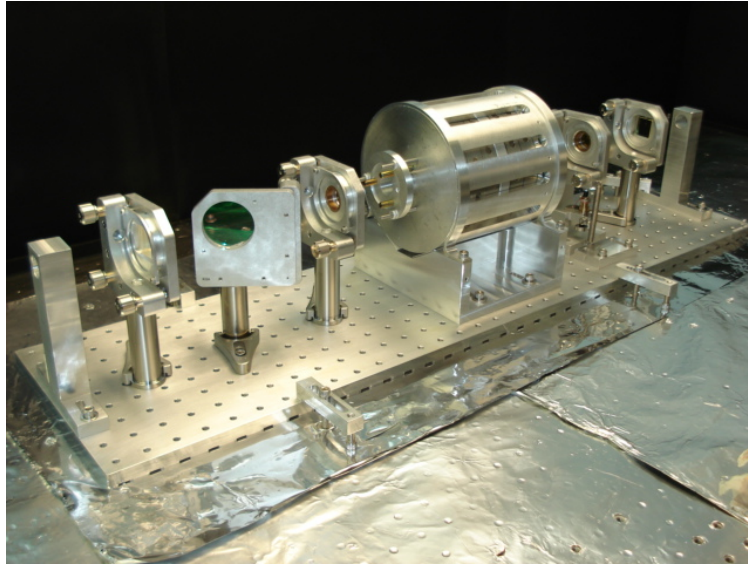
Figure 3-3. Faraday isolator. The Faraday rotator preserves the light polarization in the forward-going direction and rotates it by 90 degrees in the reverse direction. Fields are labeled for reference. Come up with better names. Overlay sketch of magnetic field strength? Show more realistic beam path angles?

3.2.3.3 Polarizers

The polarizers used (two CWPs and one TFP) each offer advantages and disadvantages related to optical efficiency in one direction, optical isolation in the other direction, and thermal beam drift. The CWPs have very high extinction ratios ($> 10^5$) and high transmission (97%), contributing to good optical efficiency and isolation performance. However, the angle separating the exiting orthogonal polarizations of light is very small, on the order of 10 mrad. This requires relatively large distances to pick off the desired beams. In addition, the $4.3°$ wedge angle of

the CWPs enables thermal drift. However, the CWPs as obtained from Karl Lambrecht for the Enhanced LIGO Faraday are low absorption with expected total drift of less than 100 μrad.

The advantages of the thin film polarizer over the calcite wedge polarizer are that it exhibits negligible thermal drift at 30 W and it is operates at the Brewster angle, thus diverting the return beam in an easily accessible way. However, the TFP has a lower transmission than the CWP and an extinction ratio of only 10^3.

Thus, the combination of CWPs and a TFP combines the best of each to provide a high extinction ratio (from the CWPs) and ease of reflected beam extraction (from the TFP). The downsides that remain when using both polarizers are that there is still some thermal drift from the CWPs. Also the transmission is reduced due to the TFP and to the fact that there are 16 surfaces from which light can scatter.

3.2.3.4 Heat conduction

In an attempt to conduct some heat away from the Faraday components, we wrapped the TGGs with indium foil that made contact with the rotator housing. We also cushioned the DKDP and HWP with indium wire in their holders.

3.2.4 Mode matching telescope

The mode matching telescope is a set of three suspended concave mirrors that direct the light transmitted through the mode cleaner and Faraday isolator to the interferometer. Located in the main vacuum system, it must provide a beam whose mode characteristics match the lowest order resonant mode of the interferometer arm cavities. The MMT must also deliver the light to the interferometer without introducing beam jitter. Design considerations are discussed in Ref. [20].

3.3 Input Optics performance

Perhaps the most convincing figure of merit for the Input Optics performance is that the Enhanced LIGO interferometers achieved low-noise operation with 20 W input power without excessive drift or other annoyances. Additionally, the Input Optics were tested successfully up to the available 30 W of power. (Instabilities with other interferometer subsystems limited

	Livingston	Hanford
Mode cleaner visibility	92%	97%
Mode cleaner transmission	88%	90%
Faraday transmission	93%	94.4%
- Thin film polarizer loss	4.0%	2.7%
IO efficiency (PSL to RM)	75%	82%

Table 3-1. Enhanced LIGO Input Optics power budget.

the operation to 20 W.) We present in this section details of the Input Optics performance during Enhanced LIGO. Specific measurements and results discussed come from Livingston; performance at Hanford was similar and is included in tables summarizing the results.

3.3.1   Optical efficiency

The optical efficiency of the Enhanced LIGO Input Optics from EOM to recycling mirror was 75%, a marked improvement over the approximate 60% of Initial LIGO. A substantial part of the improvement came simply from the discovery and subsequent correction of a 6.5% loss at one of the in-vacuum steering mirrors directing light into the MC. A 45° reflecting mirror had been accidentally used for a beam with an 8° angle of incidence. Losses attributable to the mode cleaner and Faraday isolator are described below. A summary of the IO power budget is found in Table 3-1.

3.3.1.1   Mode cleaner losses

The mode cleaner was the greatest single source of power loss in both Initial and Enhanced LIGO. The mode cleaner visibility, defined here as

$$\text{visibility} = (P_{input} - P_{reflected})/P_{input}, \tag{3.3.1}$$

the ratio of the amount of light coupled into the MC to the amount sent at it, was 92%. A result of higher order mode content and mode mismatch into the MC, the visibility was constant up to 30 W input power at both sites.

Then, of the light coupled into the mode cleaner, 88% was transmitted, corresponding to an average loss of 98 ppm per mirror. Based on the mirrors' known surface micro-roughness, the scatter loss is expected to be 22 ppm/mirror. Part of the discrepancy between expectation

28
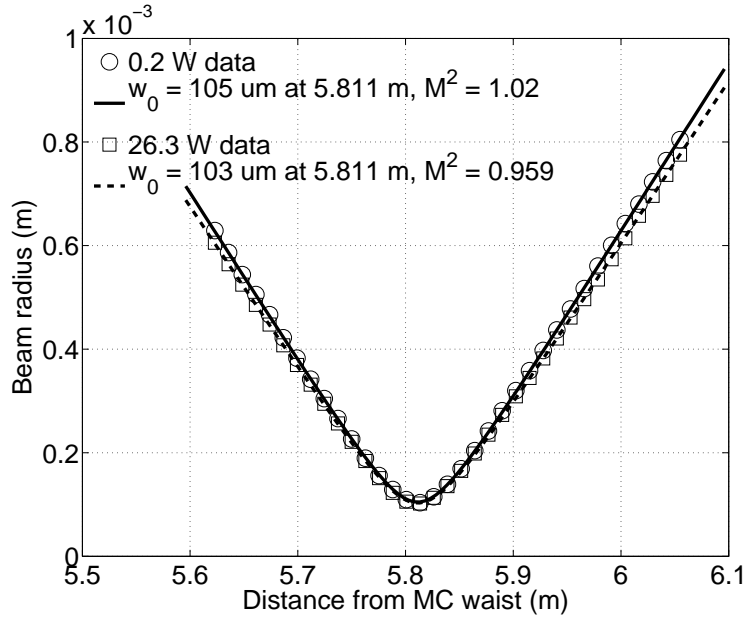
Figure 3-4. Profile at high and low powers of a pick-off of the beam transmitted through the mode celaner.

and reality comes from poor AR coatings–we measured a 1.3% reflection off the should-be AR coating on MC mirrors at both Livingston and Hanford, equivalent to a loss of 10 ppm per mirror. In addition, a scan of the beam transmitted through the mode cleaner gives M^2 values of less than 1 (see Fig. 3-4), providing evidence for clipping. In fact, MC2 has only a 1 inch clear aperture; minor decentering can create losses.

Another source of MC losses is through absorption of heat by particulates on the mirror's surface. Drag wiping the mirrors upon the completion of Initial LIGO proved beneficial. The absorption decreased from 18.7, 5.5 and 12.8 ppm per mirror, respectively, to 2.1, 2.0, and 3.4 ppm per mirror.

The measurement technique makes use of the thermally driven 28.2 kHz drumhead eigen-frequencies (Fig. 3-5) of the mirror substrate which serve as a monitor of the MC absorption via the substrate's dY/dT. We cycled the power into the mode cleaner between 0.9 W and 5.1 W at 3 hour intervals, allowing for thermal equilibrium. At the same time, we record the frequencies

Table 3-2. Mode cleaner drumhead mode shift and absorption information.

mirror	frequency	frequency shift	absorption
MC1	28.164 kHz	0.043 Hz/W	2.1 ppm
MC2	28.207 kHz	0.043 Hz/W	2.0 ppm
MC3	28.237 kHz	0.072 Hz/W	3.4 ppm

Table 3-3. Absorption values for the Livingston and Hanford mode cleaners before and after drag wiping. (For Hanford, association to a specific mode cleaner mirror is arbitrary.)

mirror	Livingston		Hanford	
	before	after	before	after
MC1	18.7 ppm	2.1 ppm	6.1 ppm	5.8 ppm
MC2	5.5 ppm	2.0 ppm	23.9 ppm	7.6 ppm
MC3	12.8 ppm	3.4 ppm	12.5 ppm	15.6 ppm

of the high Q drumhead mode peaks as found in the mode cleaner frequency error signal, heterodyned down by 28 kHz. Correcting for ambient temperature fluctuations, we find a frequency shift of 0.043, 0.043, and 0.072 Hz/W. Refer to Tables 3-2 and 3-3 and Figure 3-6. A COMSOL model relates frequency shift to absorption.

3.3.1.2 Faraday isolator losses

The Faraday isolator was the second greatest source of power loss with a transmission of 93%, better than the 86% transmission of the Initial LIGO FI. As expected, the lossiest element in the Faraday isolator was the thin film polarizer, accounting for 4% of total losses.

3.3.2 Faraday isolation ratio

The isolation ratio is defined as the ratio of power incident on the Faraday in the backwards direction to the power transmitted in the backwards direction:

$$\text{isolation ratio} = 10 \log_{10}(P_{in}/P_{out}) \qquad (3.3.2)$$

We measured the isolation ratio of the Faraday isolator *in situ* through the use of two pick-offs of the backwards transmitted beam: one was sent out of a vacuum chamber viewport immediately after transmission through the Faraday and the other was picked off in air further downstream just before entering the EOM in the backwards direction. We misaligned the interferometer arms so that the input beam would be promptly reflected off of the recycling mirror, thus subjecting
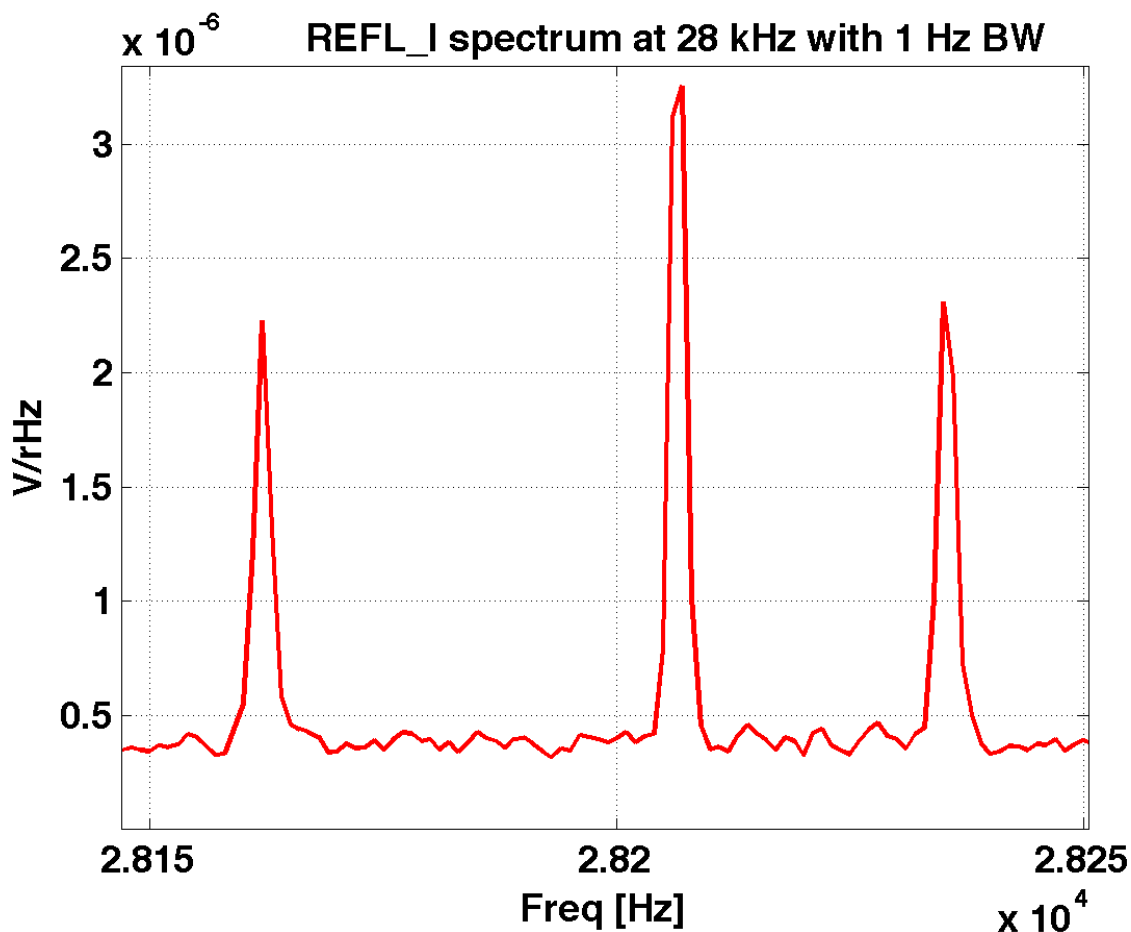
Figure 3-5. MC drumhead mode peaks. This is Rana's plot; we don't have the original data. This is a png.

the Faraday rotator to twice the input power for this measurement. As found in Figure 3-7, measurements at 1 W, 10 W, and 20 W input power show slight degradation of the Faraday's isolation performance. We report a nominal in-vacuum isolation of 26 dB. For comparison, the isolation ratio as measured in-air up to 25 W input power prior to installation was 34.4 dB.

3.3.3 Thermal drift

We measured the *in situ* thermal drift of both the beam transmitted through the mode cleaner and of the Faraday isolator up to 30 W input power. We misaligned the interferometer arms so that the input beam would be promptly reflected off of the recycling mirror, thus subjecting the Faraday rotator to 60 W total power for this measurement.
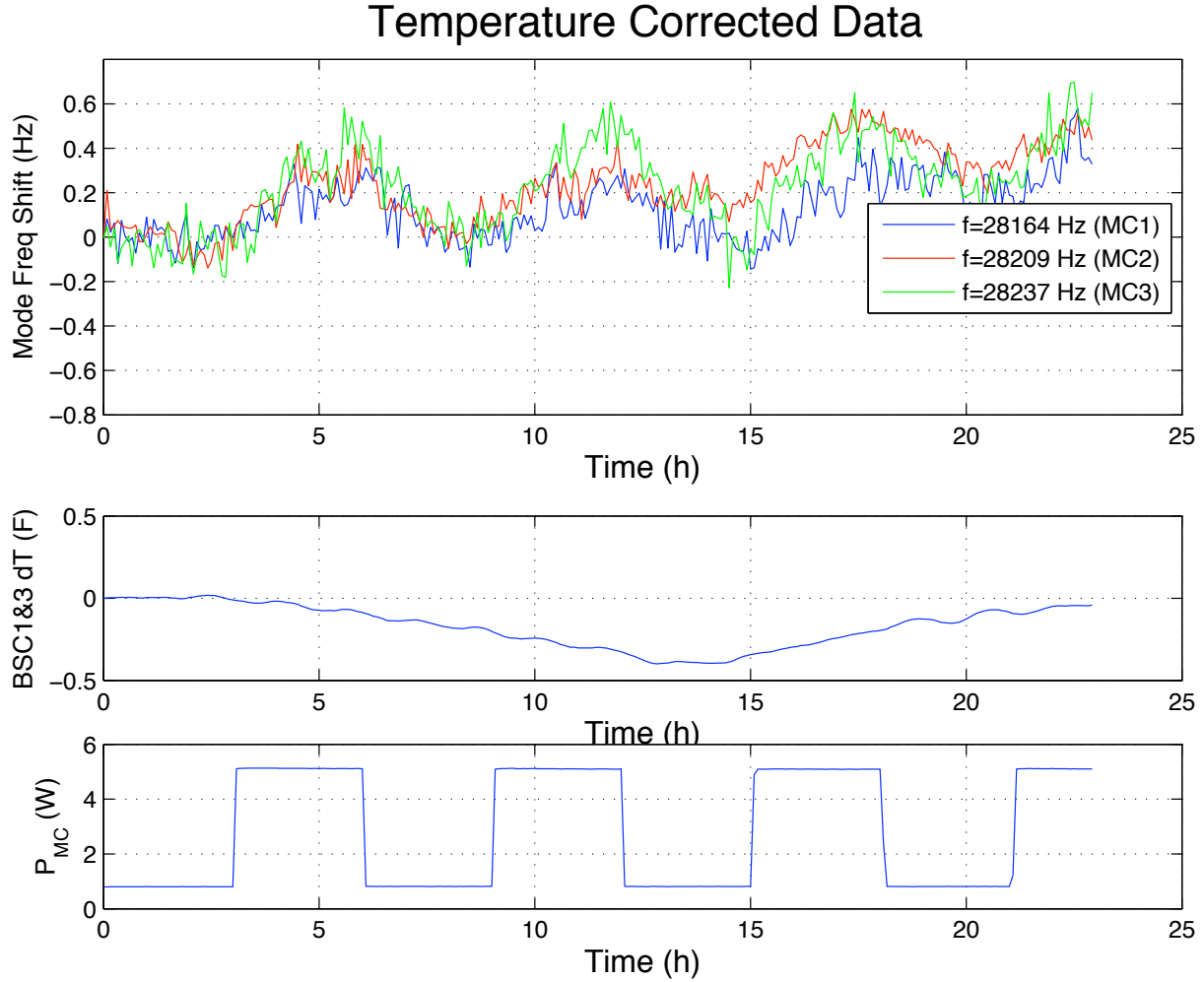
Figure 3-6. Mode cleaner absorption measurement. This is Valera's plot; we don't have original data. This is a pdf. This exact data set does *not* correspond to the data reported in Table 3-2, but that table displays the cleanest analysis we have.

As shown in Figure 3-8, the angle of the beam out of the mode cleaner does not change as a function of power in yaw and changes by 4.4×10^{-7} rad/W in pitch. (pitch and yaw reversed?) Tracking the backwards traveling beam rejected by the Faraday isolator, we record a beam drift originating at the Faraday rotator of 1.8×10^{-6} rad/W in yaw and 3.2×10^{-6} rad/W in pitch, also in Figure 3-8. Therefore, when ramping the input power up to 30 W during a full interferometer lock, the upper limit on the drift experienced by the reflected beam is about 100 μrad. The active beam steering system that had been required in Initial LIGO was no longer necessary in Enhanced LIGO.
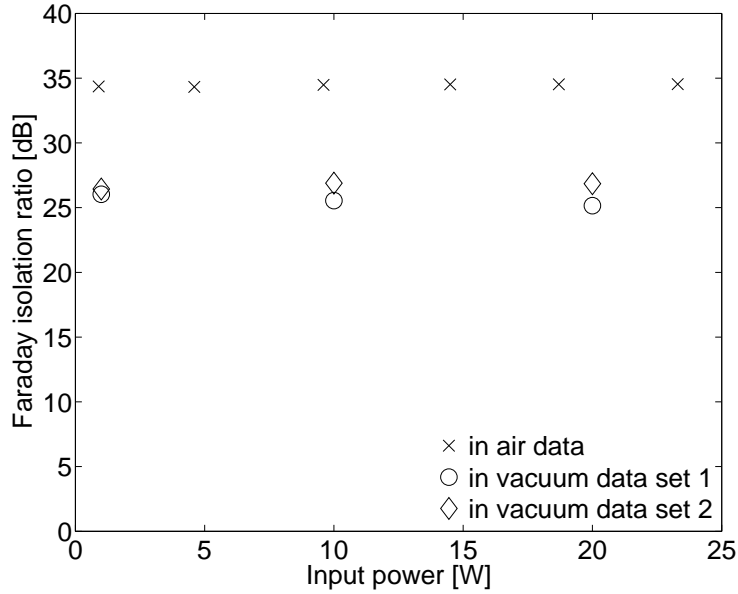
Figure 3-7. Faraday isolator isolation ratio as measured in air prior to installation and *in situ* in vacuum.

3.3.4 Thermal lensing

Using a ThorLabs WM100 Omega Meter, we measured the profile of the beam rejected by the Faraday isolator at low (1 W) and high (25 W) input power. As for the thermal drift measurement, we misaligned the interferometer arms so that the input beam would be promptly reflected off of the recycling mirror. Picking off a fraction of the beam on the in-air reflected port table, we measured the beam diameter at several locations on either side of a beam waist. Refer to Fig. 3-9 for a diagram of our measurement setup. A change in the beam waist size or position from one power to the next would indicate the presence of a thermal lens in the Faraday isolator.

As seen in Fig. 3-10, the waists of the two sets of data are collocated–no thermal lens is measured. However, the divergence of the beams differs, indicating that the beam quality degrades with higher power. The M^2 factor at 1 W is 1.04 indicating the beam is nearly perfectly a TEM$_{00}$ mode. At 25 W, M^2 increases to 1.19, corresponding to increased higher order mode content. The percentage of power in higher order modes depends strongly on the mode order and relative phases of the modes, and thus cannot be determined from this measurement [21].
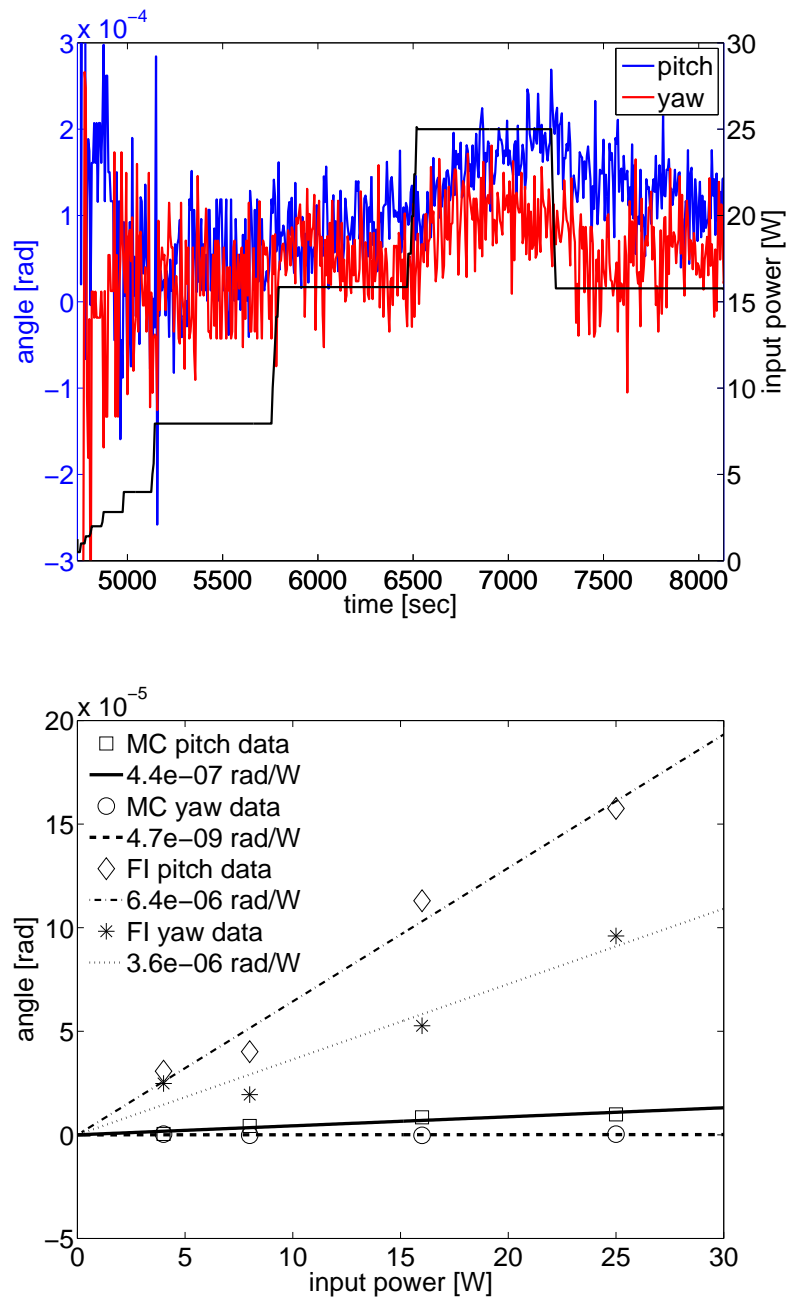
Figure 3-8. Upper plot: FI drift data. Lower plot: Reduced mode cleaner and Faraday isolator thermal drift data. Since the beam travels twice through the Faraday isolator for this measurement, FI rad/W slopes should be divided by two.

Thermal lensing measurement setup
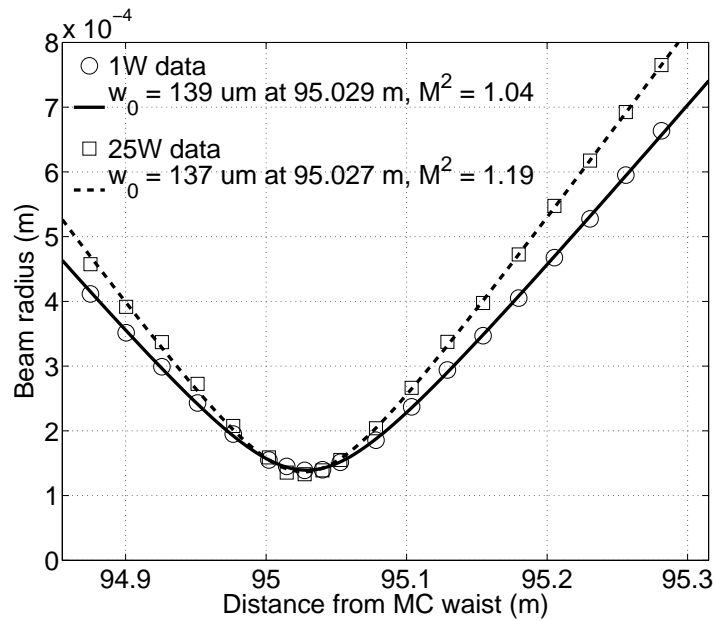
Figure 3-9. Thermal lensing measurement setup.

Figure 3-10. Faraday isolator thermal lensing data. With 25 W through the Faraday isolator one way, the beam has a steeper divergence than a pure TEM_{00} beam, indicating the presence of higher order modes.

3.3.5 Mode matching

We can measure the effectiveness of the mode-matching telescope by taking the ratio of power at the reflected port when all of the interferometer cavities are on resonance to the power in the reflected beam when the cavities are unlocked. Since the impedance matching is near perfect, all light at the reflected port during interferometer lock is attributable to a mode mismatch. The ratio we measure is 8%, meaning the MMT succeeds at coupling 92% of the light into the interferometer.

3.3.6 EOM

What to say here?

3.4 Discussion

We demonstrate that the Enhanced LIGO Input Optics enable the possibility of high power interferometry without adverse side effects. Table 3-4 summarizes the IO performance in Enhanced LIGO for both Livingston and Hanford.

Table 3-4. Enhanced LIGO Input Optics performance summary.

	Livingston	Hanford
IO transmission	75%	82%
Faraday Isolation	26 dB	
Faraday thermal drift	3 μrad/W	not measured
IO thermal lensing	negligible	not measured
Mode matching	92%	
Something else		

An important function of Enhanced LIGO was the demonstration of prototype Advanced LIGO technologies. The Enhanced LIGO Input Optics served just that purpose. Although they were subjected to at most only 20 W of input power on a regular basis, the improved performance over the Initial LIGO IO operating at 7 W input power proves the success of their design.

The Input Optics still, however, needs to work just as well with 10 times more power for Advanced LIGO. Neither the mode cleaner nor EOM showed any degradation, so projections to Advanced LIGO cannot be made. (mode cleaner radiation pressure effects?) Mode matching was constant with power, as was mode cleaner visibility and the Faraday isolation ratio. Given a Faraday isolator thermal drift of 3 μrad/W, we can expect 600 μrad/W drift in Advanced LIGO. More higher order mode content will also be generated.

CHAPTER 4
ALIGNING THE INTERFEROMETER

4.1   Introduction

The Angular Sensing and Control (ASC) subsystem uses a set of quadrant photodiodes, RF electronics, digital filters, and coil actuators to both sense and correct for the angular motion of the interferometer mirrors. Requirements for performance are stringent as too little control increases the susceptibility to lock losses and too much control decreases the interferometer's strain sensitivity. This chapter will lay out the foundations for understanding angular sensing and control in the context of Enhanced LIGO and Chapter 5 will present the results of a set of measuremets characterizing the Enhanced LIGO ASC performance.

4.1.1   Layout

There are four main subsets of sensor systems for the ASC:

- wavefront sensors (WFS1, WFS2, WFS3, WFS4)
- quadrant photodiodes (QPDX, QPDY)
- optical levers (MMT3, RM, BS, ITMX, ITMY, ETMX, ETMY)
- camera image (BS)

All but the wavefront sensors provide quite straightforward measures of angular motion. The optical levers are local to each large optic, for instance, and provide a record at all times of pitch and yaw pointing of each mirror with respect to the ground. The video camera monitors the location of the spot on the beam splitter, thus serving as a sensor of the directionality of the input beam. The two QPDs look at the light transmitted through each arm cavity, indicating the modal axis of each cavity.

Finally, the wavefront sensors provide the most sophisticated

The most primitive sensor is that of the physical video camera. The image of the speckle of light reflected off of the beam splitter (see Fig. 4-1) is fed into a labview program which integrates the intensity of the image to identify the coordinates of the center of the beam spot. This is compared with a hardcoded desired center location and a mirror upstream (MMT1) is
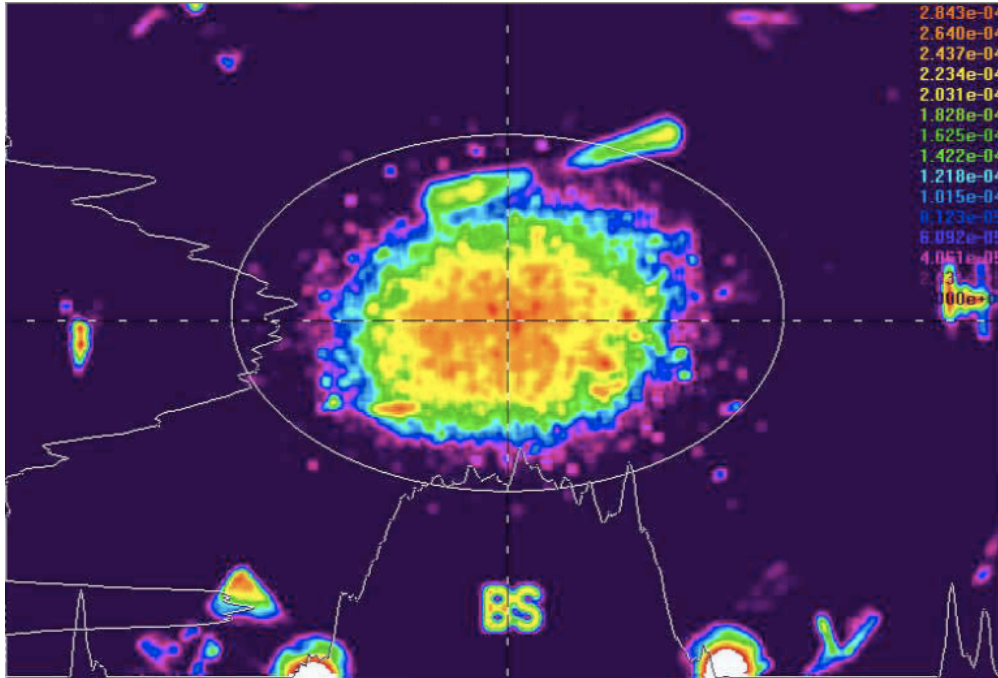
Figure 4-1. Image of beam on beam splitter as used for the beam centering servo.

moved to redirect the input beam, minimizing the difference between the desired and actual beam spot location on the BS.

4.1.2 Optical levers

The optical lever is a HeNe laser beam that reflects off of the mirror and onto a QPD. Both the laser and QPD are mounted on heavy piers to reduce the seismic noise contribution to the QPD signal. The purpose of the optical lever is to sense the mirror's motion relative to the ground and to provide a feedback signal to the mirror's coils to reduce the sensed motion. Each large optic has its own independent optical lever loop which is almost always on, even when the interferometer is out of lock. The optical lever loops provide the second level of controlled stabilization of the mirrors, after only the local damping.

- layout

- loopology

- role of optical levers

4.2 Wave-front Sensors

- hardware

- theory

4.3 Cavities with radiation pressure

- cavity eigenfunctions

- mirror torque

- cavity misalignment

- opto-mechanical transfer functions

- hard and soft modes

- Eiichi's work

4.4 Enhanced LIGO ASC design

- change of basis (Lisa's work)

- filters

CHAPTER 5
ALIGNMENT PERFORMANCE AT HIGH LASER POWER

5.1 Beam spot motion

- calibration

- residuals, perhaps for different kinds of seismic

5.2 Angular mirror motion

When the gain is really high, comparing the calibrated error and control signals shows just what the control loop is doing. The error is the residual and the control is what there would be without the loop.

error * (1+G) is the motion without the loop, where G is the open loop gain.

- optical lever calibration

- residuals, perhaps for different kinds of seismic

- compare to mirror motion with no ifo (demonstrate ASC suppression)

5.3 Open loop gains and opto-mechanical TFs

- explain measurement

- show plots

5.4 Heating related measurements

- effect of PRC g-parameter on ASC sensing matrix

- SPOB power scaling

5.5 DC readout related measurements

- RF created from DC offset beam moving on WFS1

- RF vs DC vs power comparison of (AS) beam spot motion on WFS1

5.6 ASC noisebudget

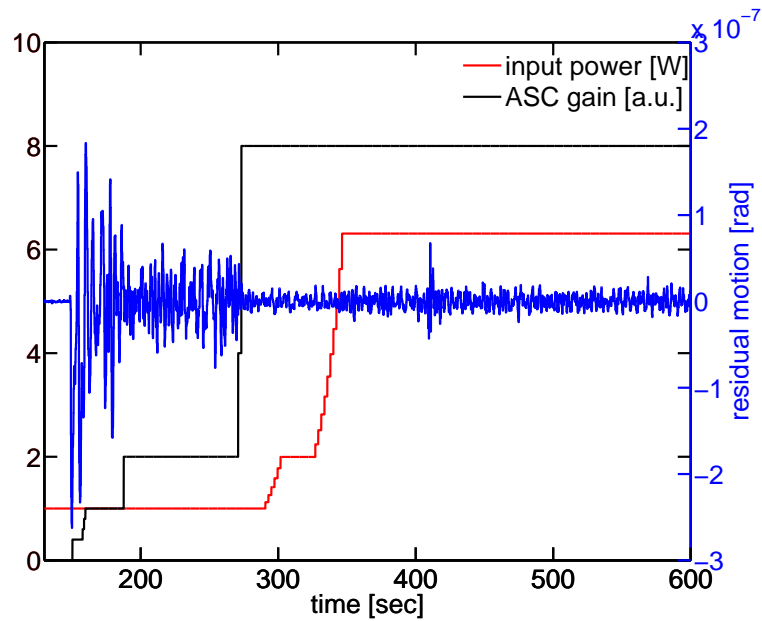- seismic - breakdown of soure of motion

- L2A

Figure 5-1. Differential unstable residual cavity motion as the ASC gain is ramped up.

- input beam

- electronics noise

- shot noise

5.7   ASC to DARM noisebudget

- describe ASC/optical lever measurement

- show results

- input beam motion to DARM

The cut-off frequency of the lowpass filters for the WFS control are of particular importance in the DARM noisebudget. The lowpass filter is necessary for suppressing the impression of sensing noise on suspension control.
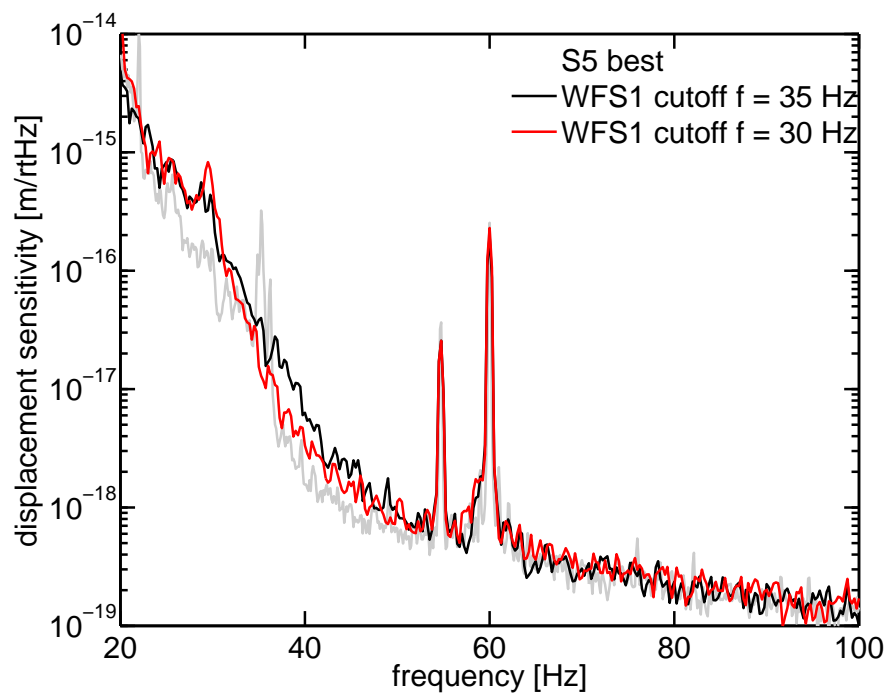
Figure 5-2. Effect of the WFS1 lowpass filter cutoff frequency on strain sensitivity.

CHAPTER 6
PROSPECTS FOR ADVANCED LIGO

6.1 Subtracting Seismic Noise from ASC

- Wiener filtering

- contributions to error signals and subtraction

- considerations for weighting filter

- feed-forward potential for aLIGO

6.2 Filtering ASC out of DARM

- convolution of beam spot motion with mirror motion

- subtraction from DARM

- post-processing or feed-forward of aLIGO data

6.3 Model of aLIGO ASC with no PRM

- aLIGO design compared to eLIGO

- Optickle aLIGO model

- error signals

CHAPTER 7
SUMMARY

REFERENCES

[1] P. Linsay, P. Saulson, R. Weiss, and S. Whitcomb, Tech. Rep. T830001, Massachusetts Institute of Technology (1983).

[2] B. P. Abbott, R. Abbott, R. Adhikari, P. Ajith, B. Allen, G. Allen, R. S. Amin, S. B. Anderson, W. G. Anderson, M. A. Arain, et al., Reports on Progress in Physics **72**, 076901+ (2009), ISSN 0034-4885, URL http://dx.doi.org/10.1088/0034-4885/72/7/076901.

[3] F. Acernese, P. Amico, M. Alshourbagy, F. Antonucci, S. Aoudia, P. Astone, S. Avino, L. Baggio, G. Ballardin, F. Barone, et al., Journal of Optics A: Pure and Applied Optics **10**, 064009+ (2008), ISSN 1464-4258, URL http://dx.doi.org/10.1088/1464-4258/10/6/064009.

[4] H. Lück, M. Hewitson, P. Ajith, B. Allen, P. Aufmuth, C. Aulbert, S. Babak, R. Balasubramanian, B. W. Barr, S. Berukoff, et al., Classical and Quantum Gravity **23**, S71 (2006), ISSN 0264-9381, URL http://dx.doi.org/10.1088/0264-9381/23/8/S10.

[5] R. Adhikari, P. Fritschel, and S. Waldman, Tech. Rep. T060156, LIGO Laboratory (2006), URL https://dcc.ligo.org/cgi-bin/DocDB/ShowDocument?docid=7384.

[6] H. Lück, C. Affeldt, J. Degallaix, A. Freise, H. Grote, M. Hewitson, S. Hild, J. Leong, M. Prijatelj, K. A. Strain, et al., Journal of Physics: Conference Series **228**, 012012+ (2010), ISSN 1742-6596, URL http://dx.doi.org/10.1088/1742-6596/228/1/012012.

[7] Advanced LIGO Systems Group, Tech. Rep. T010075, LIGO Laboratory (2009), URL https://dcc.ligo.org/cgi-bin/DocDB/ShowDocument?docid=5489.

[8] T. Fricke, N. Smith, R. Abbott, R. Adhikari, K. Dooley, M. Evans, P. Fritschel, V. Frolov, K. Kawabe, and S. Waldman, in preparation (2011), URL https://dcc.ligo.org/cgi-bin/private/DocDB/ShowDocument?docid=8442.

[9] J. S. Kissel, Ph.D. thesis, Louisiana State University (2010).

[10] M. Frede, B. Schulz, R. Wilhelm, P. Kwee, F. Seifert, B. Willke, and D. Kracht, Opt. Express **15**, 459 (2007), URL http://dx.doi.org/10.1364/OE.15.000459.

[11] J. Sidles and D. Sigg, Physics Letters A **354**, 167 (2006), ISSN 03759601, URL http://dx.doi.org/10.1016/j.physleta.2006.01.051.

[12] E. Hirose, K. Kawabe, D. Sigg, R. Adhikari, and P. R. Saulson, Appl. Opt. **49**, 3474 (2010), URL http://dx.doi.org/10.1364/AO.49.003474.

[13] L. Barsotti and M. Evans, Tech. Rep. T080186, LIGO Laboratory (2009).

[14] D. Garfinkle (2005), gr-qc/0511083, URL http://arxiv.org/abs/gr-qc/0511083.

[15] J. Camp, D. Reitze, and D. Tanner, Tech. Rep. T960170, LIGO Laboratory (1996), URL https://dcc.ligo.org/cgi-bin/DocDB/ShowDocument?docid=28745.

[16] P. Fritschel, R. Bork, G. González, N. Mavalvala, D. Ouimette, H. Rong, D. Sigg, and M. Zucker, Appl. Opt. **40**, 4988 (2001), URL http://dx.doi.org/10.1364/AO.40.004988.

[17] *Electro-Optic Modulators and Modulation for Enhanced LIGO and Beyond* (Optical Society of America, 2008), URL http://www.opticsinfobase.org/abstract.cfm?id=169025.

[18] M. Zucker, Tech. Rep. T020113, LIGO Laboratory (2002), URL https://dcc.ligo.org/cgi-bin/DocDB/ShowDocument?docid=27031.

[19] E. Khazanov, N. F. Andreev, A. Mal'shakov, O. Palashov, A. K. Poteomkin, A. Sergeev, A. A. Shaykin, V. Zelenogorsky, I. A. Ivanov, R. Amin, et al., IEEE Journal of Quantum Electronics **40**, 1500 (2004), ISSN 0018-9197, URL http://dx.doi.org/10.1109/JQE.2004.834766.

[20] T. Delker, R. Adhikari, S. Yoshida, and D. Reitze, Tech. Rep. T970143, LIGO Laboratory (1997), URL https://dcc.ligo.org/cgi-bin/DocDB/ShowDocument?docid=28875.

[21] P. Kwee, F. Seifert, B. Willke, and K. Danzmann, The Review of scientific instruments **78** (2007), ISSN 0034-6748, URL http://dx.doi.org/10.1063/1.2754400.

BIOGRAPHICAL SKETCH

Kate's biography.